



# Reconstruction of Plasma Structure with Anisotropic Pressure: Application to Pc5 Compressional Wave

Anmin Tian<sup>1</sup> , Kai Xiao<sup>1</sup>, Alexander William Degeling<sup>1</sup>, Quanqi Shi<sup>1</sup>, Jong-Sun Park<sup>1</sup>, Motoharu Nowada<sup>1</sup>, and Timo Pitkänen<sup>1,2</sup>

<sup>1</sup>Shandong Key Laboratory of Optical Astronomy and Solar-Terrestrial Environment, School of Space Science and Physics, Institute of Space Sciences, Shandong University, Weihai, Shandong 264209, People's Republic of China; [tamin@sdu.edu.cn](mailto:tamin@sdu.edu.cn)

<sup>2</sup>Department of Physics, Umeå University, Umeå, Sweden

Received 2019 September 10; revised 2019 December 7; accepted 2019 December 14; published 2020 January 23

## Abstract

The conventional Grad–Shafranov (GS) method is designed to reconstruct a two-dimensional magnetohydrostatic structure with isotropic pressure. In this work, we developed a new GS solver (GS-like) that includes the effect of pressure anisotropy based on reduced equations from Sonnerup et al. The new GS solver is benchmarked, and the results are compared with two other GS solvers based on the conventional GS method and that from Teh. This solver is applied to reconstruct a Pc5 compressional wave event, which has mirror-like features and includes a significant pressure anisotropy ( $p_{\perp}/p_{\parallel} \sim 1.5$ , where  $p_{\perp}$  and  $p_{\parallel}$  are the thermal pressures perpendicular and parallel to the magnetic field), observed by the Magnetospheric Multiscale mission in the duskside outer magnetosphere on 2015 September 19. The recovered maps indicate that, within some model constraints, the wave in the selected time interval consists of two magnetic bottle-like structures, each with an azimuthal size of about 9000 km (wavenumber  $\sim 44$ ) and a larger field-aligned size. The spacecraft passed through the bottles at  $\sim 1600$  km southward of the bottle centers. Further multispacecraft measurements revealed that the Pc5 compressional wave propagates sunward along with the background plasma and retains the bottle-like structures, driven mainly by the ion diamagnetic currents. The reconstructed magnetic topology is similar to that described in previous empirical or theoretical antisymmetric standing wave models. This Pc5 compressional wave is possibly driven by drift-mirror-like instabilities.

*Unified Astronomy Thesaurus concepts:* Planetary magnetosphere (997); Space plasmas (1544)

## 1. Introduction

Pc5 ultra-low-frequency waves with frequency 1.6–6.7 mHz are commonly observed in Earth's magnetosphere, playing important roles in energy transport and the modulation and acceleration of charged particles in the inner magnetosphere (e.g., Zong et al. 2007, 2009; Yang et al. 2010; Jing et al. 2014). These waves generally exist in the form of cavity mode/waveguide modes (fast mode waves) or shear Alfvén modes by field-line resonances and are excited by solar wind disturbances or internal instabilities (e.g., Lu et al. 2003; Shi et al. 2013). Different from the above magnetohydrodynamic (MHD) waves, the Pc5 compressional waves studied in this work have special features in that they are prone to occurring in the high plasma  $\beta$  (ratio of thermal pressure to magnetic pressure) and high temperature anisotropy plasma environment in the outer magnetosphere (Takahashi et al. 1985, 1987a, 1987b; Zhu & Kivelson 1991, 1994; Korotova et al. 2009, 2013). The magnetic and thermal pressures in these waves nearly balance each other (e.g., Vaivads et al. 2001). Using the timing method with multiple spacecraft or finite gyroradius techniques, it was found that these waves propagate sunward at speeds of tens of  $\text{km s}^{-1}$ , with azimuthal wavelength of 0.5–5 Earth radii ( $R_E$ ; e.g., Takahashi et al. 1987b; Vaivads et al. 2001; Constantinescu et al. 2009). Their generation is still a controversial issue. The most popular generation mechanism is the drift-mirror mode driven by temperature anisotropy (e.g.,  $T_{\perp} > T_{\parallel}$ ; Hasegawa 1969). “Mirror mode” refers to nonoscillating magnetic structures frozen into the plasma (e.g., Kivelson & Southwood 1996), and the above theory suggests that the drift-mirror mode propagates slowly because of the effect of density and magnetic field gradients. For some wave events, the phase velocity is close

to the background plasma velocity (e.g., Vaivads et al. 2001). Modified versions of the drift-mirror mode theory that take into account the magnetic field-line curvature and coupling with transverse waves (e.g., Cheng & Qian 1994), bounce-drift resonances (Southwood et al. 1969), and the slow mode have also been proposed as possible generation mechanisms. However, slow mode waves usually damp heavily under typical magnetospheric plasma conditions (Su et al. 1980).

The wave structures are of great interest for the understanding of particle acceleration/modulation processes and the generation mechanisms of the waves (e.g., Sibeck et al. 2012). It has been found that the Pc5 compressional wave exhibits an antisymmetric standing wave structure along the ambient field line with its node near the magnetic equatorial plane (Takahashi et al. 1987a; Cheng & Qian 1994; Haerendel et al. 1999; Vaivads et al. 2001). Considering a two-dimensional (2D) divergence-free condition, a field configuration model proposed by Takahashi et al. (1987a) showed that the compressional signals are related to the azimuthal compression or expansion of magnetic flux tubes. The formed magnetic “bottle-like” structure involving a lower magnetic field strength and higher particle flux alternates along the azimuthal direction in the northern and southern hemispheres. A magnetic bottle has also been considered as the typical topology of the magnetic holes observed in the spatial plasma (e.g., Xiao et al. 2010; Yao et al. 2017). The wavelength in the azimuthal direction (several  $R_E$ ) has been widely acquired using the finite gyroradius technique or the timing method (e.g., Su et al. 1977; Constantinescu et al. 2009). However, the field-aligned size and profile are rarely studied by observations, due to the limited spatial coverage of spacecraft (Takahashi et al. 1987a; Korotova et al. 2013).

Tian et al. (2012) had reconstructed a Pc5 compressional wave event with pressure isotropy using the conventional Grad–Shafranov (GS) reconstruction method. The conventional GS reconstruction method, which has successfully recovered the geometry of magnetopause, magnetotail flux ropes, and magnetic clouds (Sonnerup & Guo 1996; Hau & Sonnerup 1999; Hu & Sonnerup 2002, 2003; Hasegawa et al. 2005, 2007), is made available for a quasi-2D and pressure-isotropic MHD structure. But for most Pc5 compressional waves, the plasma has remarkable anisotropy, such that  $p_{\perp}$  is much larger than  $p_{\parallel}$  (e.g., Zhu & Kivelson 1994; Korotova et al. 2009). Taking double-polytropic laws as energy closure, together with the momentum equation, Sonnerup et al. (2006) deduced a GS-like equation including effects of both pressure anisotropy and field-aligned flow. An auxiliary  $9 \times 9$  equation set is required to perform the reconstruction. The corresponding GS-like solver was developed by Chen & Hau (2018) and first applied to a magnetopause crossing. Ignoring the field-aligned flow and only considering the pressure anisotropy, Teh (2018) obtained another GS-like equation with an integration scheme closer to the conventional GS method without resorting to an auxiliary equation set and used it to reconstruct a mirror structure in the magnetosheath (Teh 2019). However, he assumed the anisotropic factor  $\alpha$  (see the next section for the definition), a field-line invariant, which may not be necessarily applicable in a general plasma environment. In this paper, we focused on a magnetohydrostatic equilibria structure including only a pressure anisotropy effect and reduced the GS-like equation and equation set given by Sonnerup et al. (2006) to establish the GS solver. We call it the reduced GS-like method in the following sections. To evaluate our new solver, an analytical model was developed for a benchmark. In addition, another GS solver based on the method of Teh (2018) has also been established and benchmarked for comparison.

When reconstructing a mirror-like structure with practical data, the key is to find a proper frame and coordinate system, the so-called reconstruction plane (e.g., Tian et al. 2012). With observation by a single spacecraft, they are generally difficult to determine accurately (e.g., Tian et al. 2019; Shi et al. 2019). Fortunately, the wave event studied at present was observed by the Magnetospheric Multiscale mission (MMS; Burch et al. 2016), which includes four identical spacecraft, providing high time resolution magnetic field data and plasma data suitable for investigating the structure configuration and the particle behaviors (e.g., Yao et al. 2017). With magnetic field data from four spacecraft, the minimum direction derivative (MDD) method can be used to determine the dimensionality of the wave structure (Shi et al. 2005). The spatiotemporal difference analysis (STD) method (Shi et al. 2006) can then be used to calculate the velocity in each dimension and find the proper reconstruction plane.

The paper is organized as follows. Section 2 introduces the analytical model we designed and the benchmark results of three different GS solvers. Section 3 gives a brief introduction to the spacecraft and data. In Section 4, a Pc5 compressional wave event observed by MMS in the duskside magnetosphere is analyzed in detail by using the reduced GS-like method and the multispacecraft analysis method. As far as we know, this is the first time the GS-like method including a pressure anisotropic effect has been adopted to reveal the magnetospheric Pc5 compressional wave structure. The current system and the behavior of particle modulation in the wave are also

investigated. Section 5 discusses the field-aligned scale and the generation mechanisms of the wave. The last section gives a summary.

## 2. Method and Benchmark

When considering pressure anisotropy (i.e.,  $p_{\parallel} \neq p_{\perp}$ ), the magnetohydrostatic equilibria equation can be described as follows (e.g., Teh 2018):

$$\nabla \cdot [(1 - \alpha)\mathbf{B}\mathbf{B}] = \mu_0 \nabla \cdot \left( p_{\perp} + \frac{B^2}{2\mu_0} \right), \quad (1)$$

where  $\alpha = (p_{\parallel} - p_{\perp})\mu_0/B^2$  is the pressure anisotropy factor, and  $\mu_0$  is vacuum permeability. Using double-polytropic closure relations and an assumption of 2D, Equation (1) can be turned into a GS-like equation as follows:

$$\nabla \cdot [(1 - \alpha)\nabla A] = \mu_0 \rho \left[ T_{\perp} \frac{dS_{\perp}}{dA} + T_{\parallel} \frac{dS_{\parallel}}{dA} - \frac{dH}{dA} \right] - B_z \frac{dC_z}{dA}. \quad (2)$$

This equation can be obtained directly by setting the velocity to zero in Equation (A7) of Sonnerup et al. (2006), which includes effects of both field-aligned flow and pressure anisotropy. In Equation (2),  $A$  indicates the magnetic vector potential along invariant axis  $\hat{z}$ ,  $\rho$  is the mass density,  $S_{\perp} = c_{v\perp} \cdot \ln(p_{\perp}/\rho B^{\gamma_{\perp}-1})$  and  $S_{\parallel} = c_{v\parallel} \cdot \ln(p_{\parallel} B^{\gamma_{\perp}-1}/\rho^{\gamma_{\parallel}})$  are the perpendicular and parallel pseudoentropies, respectively,  $H = \frac{p_{\perp}}{(\gamma_{\perp}-1)\rho} + \frac{\gamma_{\parallel}}{\gamma_{\parallel}-1} \frac{p_{\parallel}}{\rho}$  is the total enthalpy, and  $C_z = (1 - \alpha)B_z$ . All of  $S_{\perp}$ ,  $S_{\parallel}$ ,  $H$ , and  $C_z$  are field-line invariants, which are invariant along the field line in the reconstruction plane, namely, a function of  $A$  alone. Here,  $\gamma_{\perp} = c_{p\perp}/c_{v\perp}$  and  $\gamma_{\parallel} = c_{p\parallel}/c_{v\parallel}$  are polytropic values. Usually, the choice of  $\gamma_{\perp}$  and  $\gamma_{\parallel}$  is empirical, depending on the plasma environment of concern. They are chosen as  $\gamma_{\perp} = 2$ ,  $\gamma_{\parallel} = 3$  for double-adiabatic cases and  $\gamma_{\perp} = 1$ ,  $\gamma_{\parallel} = 1$  for double-isothermal cases (e.g., Hau et al. 1993; Sonnerup & Hau 1994; Chen & Hau 2018). In kinetic theory for mirror mode, they could be  $\gamma_{\perp} = 2$  and  $\gamma_{\parallel} = 0.5$  (e.g., Chen & Hau 2018), which are adopted in the present paper for recovering the MMS observed event. Similar results were obtained by using values for the adiabatic case but with higher numerical instability. We will not discuss the impact of our choice of polytropic values in this paper, and we just focus on the understanding of the results based on using  $\gamma_{\perp} = 2$  and  $\gamma_{\parallel} = 0.5$  in practical applications. The symbols  $c_p$  and  $c_v$  denote the specific heat at constant pressure and volume, respectively. In the isothermal case,  $H$  should use the form of Equation (14) in Hau (1996) instead. Reduced auxiliary equations, containing seven equations, obtained by removing items containing velocity  $v$  in Equations A11–A14 (see the appendix of Sonnerup et al. 2006) are used to advance the seven quantities  $\alpha$ ,  $\rho$ ,  $p_{\perp}$ ,  $p_{\parallel}$ ,  $B_z$ ,  $B^2$ , and  $\partial^2 A/\partial^2 y$  when integrating Equation (2) as a spatial initial-value problem.

Chen & Hau (2018) had deduced an analytical solution of the GS-like equation including effects of both pressure

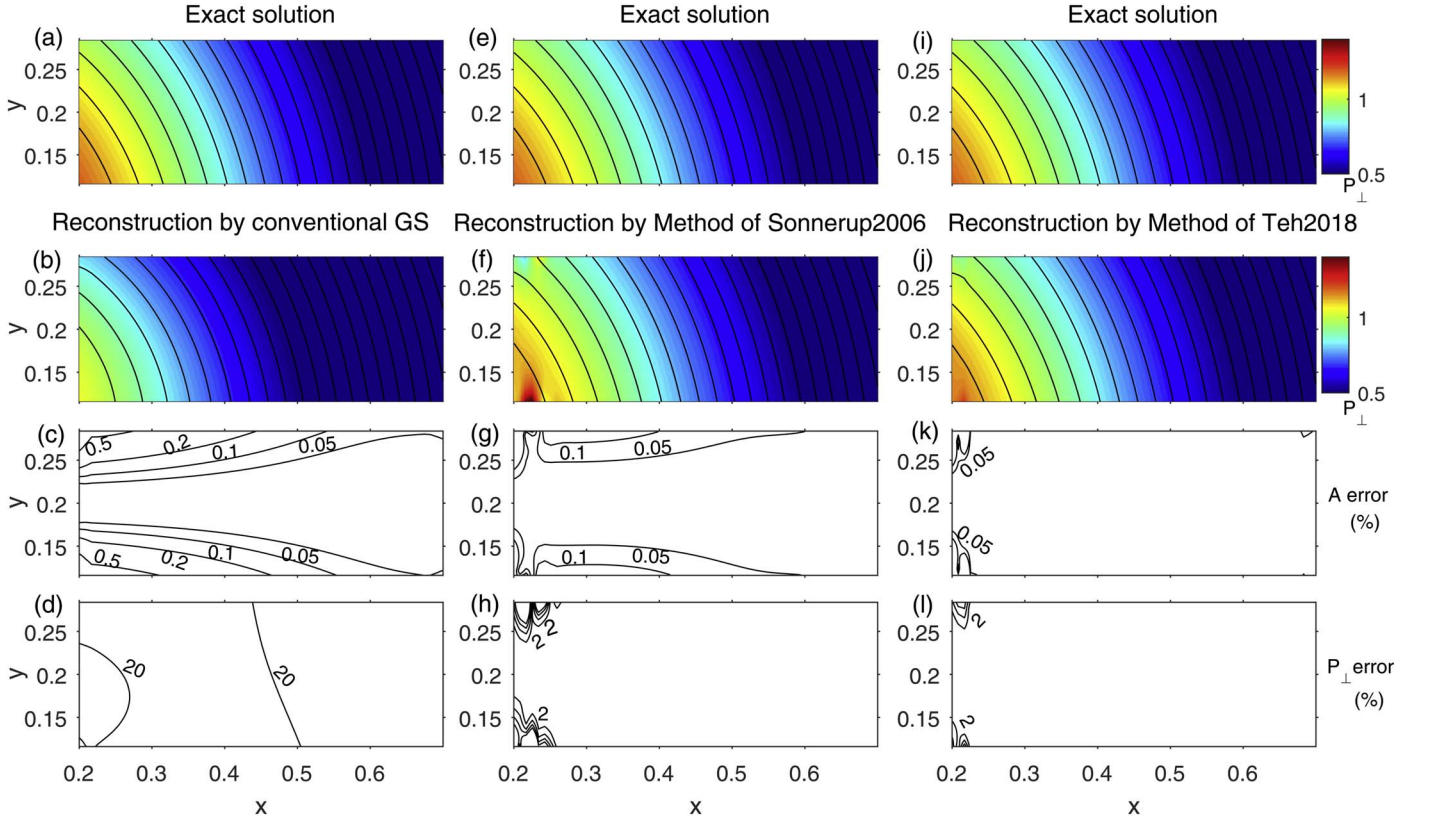


**Figure 1.** Comparison of the exact model solution with reconstruction from different methods. Panels (a), (e), and (i) are the same, denoting the exact model solution of vector potential  $A$  (black contour) with perpendicular pressure  $P_{\perp}$  in color. (b), (f), and (j) are reconstructed results from the conventional GS method, the reduced GS-like method, and the method from Teh (2018). (c), (g), and (k) are relative error contours of  $A$ , calculated by  $|A_{\text{rec}} - A_{\text{exact}}| / \langle |A| \rangle$ , where  $A_{\text{rec}}$  denotes reconstructed  $A$ ,  $A_{\text{exact}}$  denotes exact  $A$ ,  $\langle \rangle$  denotes the average over the reconstruction window. (d), (h), and (l) are relative error contours of  $p_{\perp}$  using a similar formula to get the errors of  $A$ .

anisotropy and field-aligned flow for validating their GS solver. The use of constant  $\alpha$  in their solution simplifies the integration process. Another analytical solution was developed by Teh (2018), which cannot be used to test the integration scheme of Sonnerup et al. (2006) because the mass density  $\rho$  is undefined. We derived a new axisymmetric analytical solution of Equation (2) (taking  $\gamma_{\perp} = 2$ ,  $\gamma_{\parallel} = 3$ ) to validate our codes.

Assuming  $A = B_z^2 = \rho = e^{-r^2}$ , simply making  $S_{\parallel} = \frac{C_{v\parallel}}{C_{v\perp}} \cdot S_{\perp}$  in cylindrical coordinates, and utilizing the following forms for  $\alpha = \alpha_r \cdot p_{\perp}$ ,  $T_{\perp} = T_{\perp r} \cdot p_{\perp}$ ,  $T_{\parallel} = T_{\parallel r} \cdot p_{\perp}$ ,  $S_{\perp} = S_{\perp r} + C_{v\perp} \ln p_{\perp}$ ,  $S_{\parallel} = S_{\parallel r} + C_{v\parallel} \ln p_{\perp}$ , and  $H = H_r \cdot p_{\perp}$ , we can transform Equation (2) into

$$f_1 \cdot \frac{dp_{\perp}}{dr} + f_2 \cdot p_{\perp} = f_3 \quad (3)$$

where  $f_1 = \frac{B_z^2 \alpha_r}{dA/dr} + \frac{\mu_0 \rho}{dA/dr} (T_{\perp r} C_{v\perp} + T_{\parallel r} C_{v\parallel} - H_r) + \alpha_r (dA/dr)$ ,  $f_2 = \frac{B_z}{dA/dr} \left( \frac{d\alpha_r}{dr} B_z + \alpha_r \frac{dB_z}{dr} \right) + \frac{\mu_0 \rho}{dA/dr} \left( T_{\perp r} \frac{dS_{\perp r}}{dr} + T_{\parallel r} \frac{dS_{\parallel r}}{dr} - \frac{dH_r}{dr} \right) + \frac{d\alpha_r}{dr} \frac{dA}{dr} - 4A(1 - r^2)\alpha_r$ , and  $f_3 = -4A(1 - r^2) + \frac{(dB_z/dA)B_z}{dA/dr}$ .

Then we get the solution of  $p_{\perp}$  as  $p_{\perp} = e^{-\int f_2/f_1 dr} \cdot \left[ \int \frac{f_3}{f_1} \cdot e^{\int f_2/f_1 dr} dr + C \right]$ , where  $C$  is a constant and taken to be 1.1 here. The distribution of the exact model  $p_{\perp}$  is presented in color in Figure 1(a), in which the black curves denote the exact transverse magnetic lines. Note that, in our solution,  $\alpha$  is a

function of the coordinate  $r$  alone and therefore a field-line invariant. Therefore, the newly developed solution could also be used to validate the method proposed by Teh (2018).

To facilitate comparison with the reconstruction results, Figures 1(a), (e), and (i) are plotted exactly the same with the same format. The reconstructions are conducted using data taken from the virtual path of  $y = 0.2$ . The other panels in the left, middle, and right columns show the reconstruction results and errors from the conventional GS method, the reduced GS-like method, and that from Teh (2018), respectively. It shows that, compared with the other two methods, the error of magnetic potential  $A$  recovered by the conventional GS method increases more rapidly with  $y$  away from the virtual path (Figure 1(c)), and the error became 2–4 times larger than that of the reduced GS-like method (Figure 1(g)) at  $y = 0.25$  and  $y = 0.15$ . Besides, the conventional GS method considers the pressure as isotropic, so the relative error of recovered pressure to exact  $p_{\perp}$  is as large as 20% (Figure 1(d)), whereas, for the other two methods, the relative error of  $p_{\perp}$  is less than 2% except at the left corners (Figures 1(h) and (l)). The benchmark result suggests that our reduced GS-like solver has good accuracy in the given domain. The results from Teh (2018) have the smallest errors, which is understandable because it involves a fewer number of field-line invariants and does not need to solve the equation set compared to the reduced GS-like method, resulting in smaller numerical errors.

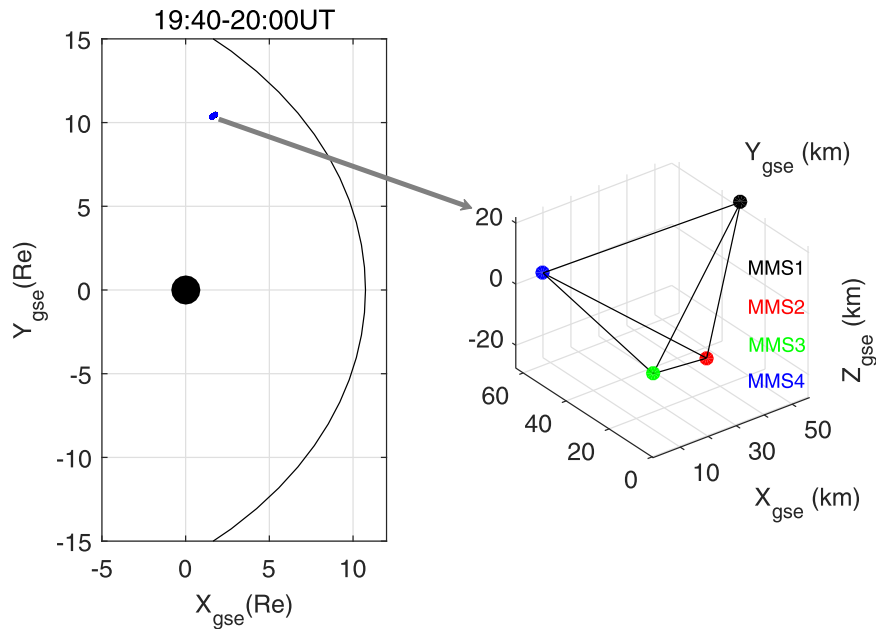


**Figure 2.** MMS position projected in the GSE  $X$ - $Y$  plane (left) and the MMS tetrahedron formation (right) during the event time interval. The black curve in the left panel indicates the magnetopause location based on the Shue et al. (1998) empirical model. In the right panel, the coordinate origin is taken as the position of MMS3 at the beginning of this time interval.

### 3. Data

In this paper, we focus on the study of a Pc5 compressional wave event observed by the MMS spacecraft on 2015 September 19. The survey-mode magnetic field data with time resolution of 0.0625 s provided by the fluxgate magnetometers (Russell et al. 2016) and fast-mode plasma data with time resolution of 4.5 s provided by the fast plasma investigation (FPI) instrument (Pollock et al. 2016) are used for analysis. The data are displayed in the Geocentric Solar Ecliptic (GSE) coordinate system except for special instructions. During the time period of interest, the four spacecraft were located at  $\sim(2.0, 10.6, -0.7)$  Re with a separation distance of  $\sim 62$  km in the duskside outer magnetosphere (see Figure 2). The 2D geometrical factors of the tetrahedron, including elongation parameter  $E$  and planarity parameter  $P$ , are 0.1814 and 0.2186, respectively. Both  $E$  and  $P$  take values between 0 and 1. The closer to 1, the more stretched ( $E$  is larger) or flattened ( $P$  is larger) the tetrahedron. The current values are much less than 1, indicating a nearly regular configuration, which is favorable for the application of multispacecraft analysis methods (Robert et al. 1998).

## 4. Event Study

### 4.1. Overview

Figure 3 shows the magnetic field and plasma data observed by MMS1 between 18:40 and 20:00 UT. After 19:10 UT, obvious compressional oscillation was observed in the total magnetic field strength  $B_t$  (Figure 3(a)). A wavelet analysis shows that the oscillation period is  $\sim 600$  s, which falls into the Pc5 domain (Figure 3(b)). The oscillation amplitude of  $B_t$  reaches 17% of the background value, indicating it is in the nonlinear stage (e.g., Kivelson & Southwood 1996). The plasma density is higher (even larger than  $1 \text{ cm}^{-3}$ ) and varies almost in phase with the ion perpendicular temperature (Figure 3(d)) and antiphase with  $B_t$  (Figure 3(a)). The ion

perpendicular temperature is  $\sim 1.5$  times larger than the parallel temperature (Figure 3(d)). The electron temperatures also exhibit notable anisotropy ( $T_{e\perp} > T_{e\parallel}$ , Figure 3(e)). The magnetic pressure and plasma thermal pressure almost balance each other, and the total pressure (magnetic pressure plus thermal pressure) is nearly constant after 19:40 UT, as shown in Figure 3(f). These characteristics suggest that the Pc5 compressional wave would have stable mirror-type structures (e.g., Hasegawa 1969; Cheng & Qian 1994; Vaivads et al. 2001). As shown in Figure 3(i), the onset criterion for mirror mode  $\beta_{\perp} \left( \frac{T_{\perp}}{T_{\parallel}} - 1 \right) > 1$  (e.g., Hasegawa 1969; Southwood & Kivelson 1993) is satisfied for half the time after 19:10 UT along with enhanced wave activity, where  $\beta_{\perp}$  equals the ratio of the perpendicular thermal pressure to the magnetic pressure. Some previous observations have found that compressional waves related to drift-mirror instability may be satisfied with this criterion just in partial time periods (e.g., Zhu & Kivelson 1994; Korotova et al. 2009). Ion flow velocity (Figure 3(g)) shows that  $V_y$  oscillates with amplitude less than  $40 \text{ km s}^{-1}$ . The electron velocity (Figure 3(h)) presents a distinct profile from the ion velocity. Aside from the electron  $V_x$  with larger offset being caused by correction of photoelectrons, the other inconsistency from the ion velocity may be physical, which will be explained in Section 3.3 by the ions being carriers of diamagnetic currents. As shown by Gershman et al. (2017), photoelectrons generated inside the instrument have a bulk velocity of  $V_{px} \sim -700 \text{ km s}^{-1}$ . To remove them, in FPI moments, an empirical normalized phase space density (PSD) model for photoelectrons has been built and multiplied by a tuning factor  $n_p$ , and then been subtracted from the actual measured PSD. The modified PSD is finally used to form various plasma moments. The electron  $V_x$  component, the most sensitive, sometimes would deviate from the ion  $V_x$  after correction.

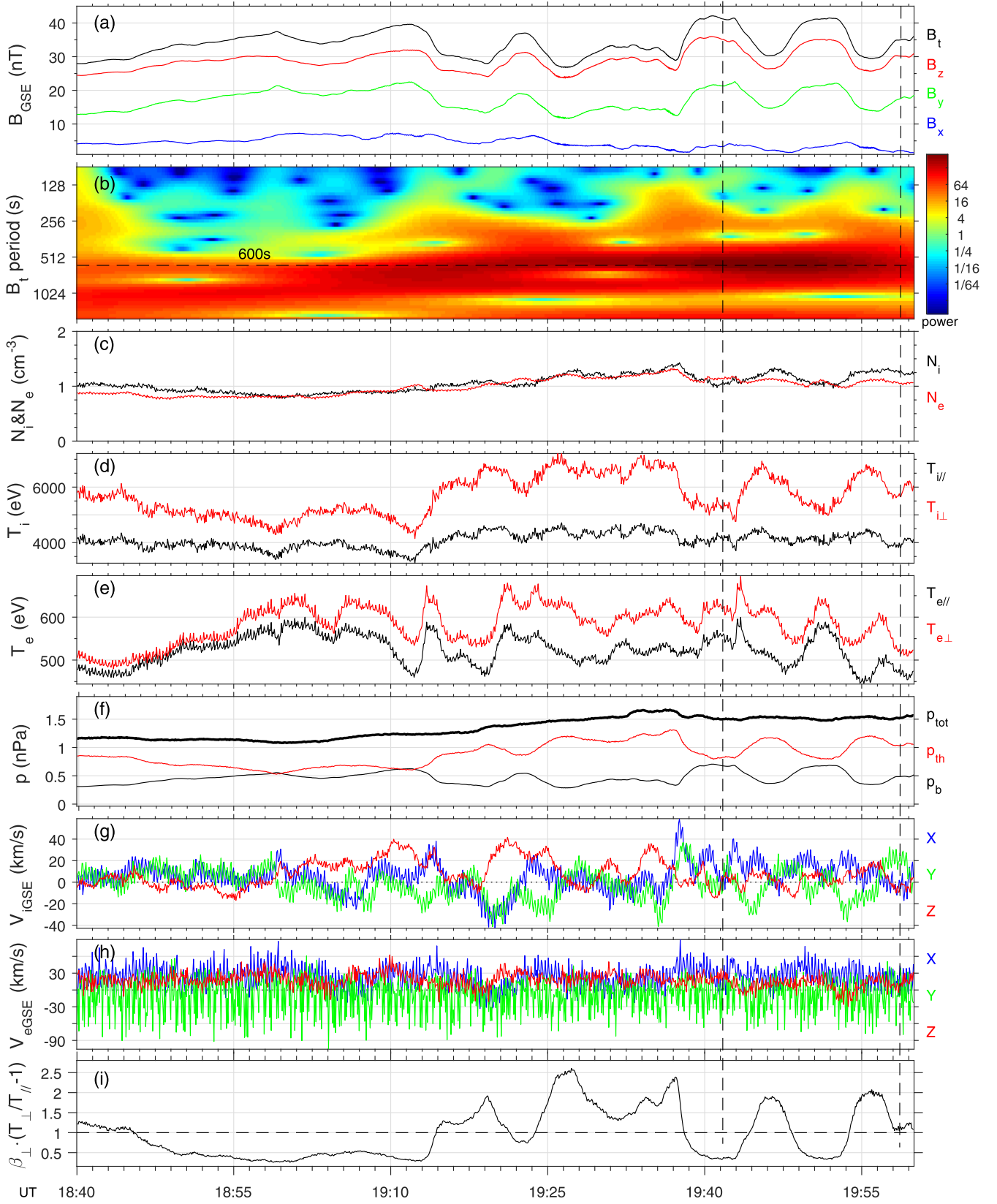


**Figure 3.** Summary plot of the Pc5 compressional wave event observed on 2015 September 19 by MMS1. From top to bottom: an overplot of magnetic field intensity ( $B_t$ ) and the three components (a); the wavelet analysis spectrum of  $B_t$  (b); ion (black) and electron (red) density (c); parallel (black) and perpendicular (red) temperature of ions (d); parallel (black) and perpendicular (red) temperature of electrons (e); an overplot of the thermal pressure ( $p_{th}$ ), magnetic pressure ( $p_b$ ), and total pressure, obtained by  $p_{tot} = p_{th} + p_b$  (f); three components of ion (g) and electron (h) velocity in GSE coordinates (h); and the criteria for mirror instability (i). The vertical dashed lines mark the time period for the reconstruction.

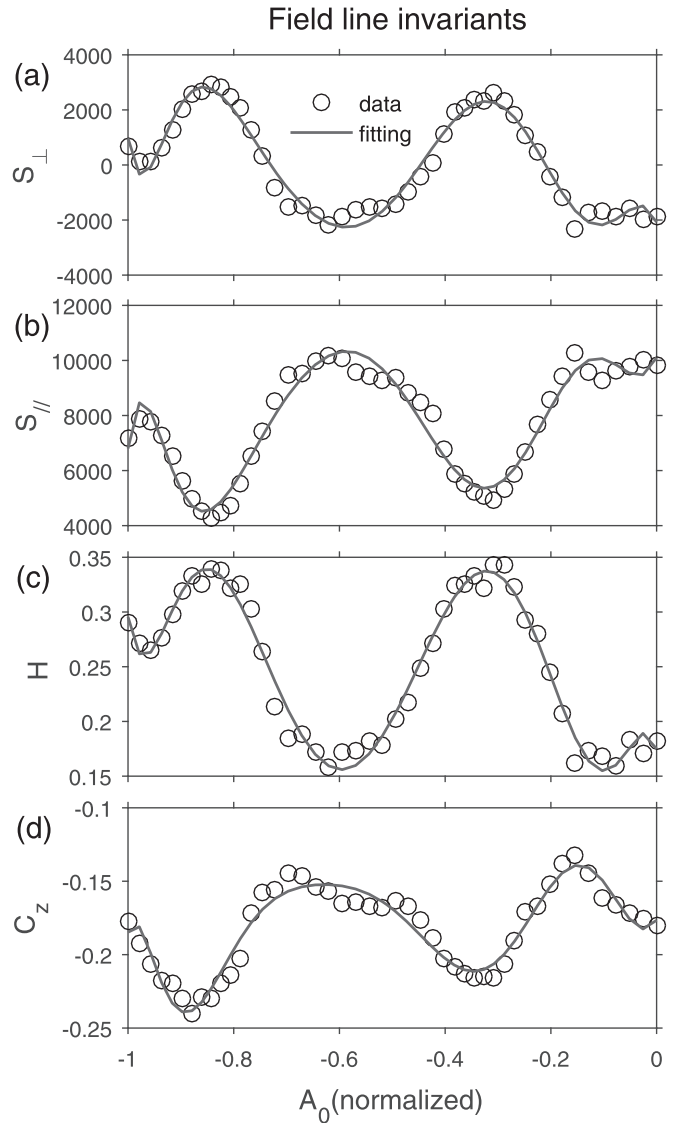
#### 4.2. Reconstruction Results

Data provided by MMS1 from 19:40:15 to 19:59:10 UT as marked by the two vertical dashed lines in Figure 3 are used for reconstruction. Since each magnetic field line in the reconstruction plane may be encountered only once by the spacecraft path, the conventional trial-and-error method based on single-spacecraft data for determining the invariant axis is not available (e.g., Hu & Sonnerup 2002; Chen & Hau 2018). Using the MDD method, it was found that the maximum gradient directions at times 19:44:00, 19:48:30, and 19:53:30 UT (boundary times) can be well determined in the case of the larger ratios of  $\sqrt{\lambda_1}/\sqrt{\lambda_2} \sim 2.6, 2.0,$  and  $3.8$ , where  $\lambda_1$  and  $\lambda_2$  denote the maximum and intermediate eigenvalues, respectively (e.g., Shi et al. 2005). These results suggest that the boundaries between the strong and weak magnetic field regions are approximately one-dimensional. Their normal vectors, nearly all along  $+x$  (close to the westward considering the spacecraft position) and perpendicular to the ambient magnetic field, are averaged to get  $N_{\max} = [0.9947, -0.0247, -0.0998]$ . Using minimum variance analysis (MVA), the direction of maximum variance of the magnetic field is further determined as  $L = [0.0925, 0.6389, 0.7637]$  with an angle of  $\sim 9.1^\circ$  from the background magnetic field. We choose the final invariant axis direction as  $k = L \times N_{\max} = [-0.0449, 0.7689, -0.6378]$  and reconstruct the relevant parameters in the  $L$ - $N_{\max}$  plane. A similar method combining MDD and MVA analysis was used by Denton et al. (2016) and Hasegawa et al. (2017) to establish a proper coordinate system. Note that a quasi-2D assumption was made because the boundaries are close to 1D and the wavelength of this type of Pc5 compressional wave is usually much larger in the radial direction than in the azimuthal direction (e.g., Zhu & Kivelson 1994; Vaivads et al. 2001).

The STD analysis (Shi et al. 2006, 2009) shows that the above three boundaries move sunward with a speed of about  $18 \text{ km s}^{-1}$  in the spacecraft frame. The averaged normal velocity  $V_{sc} = [18.1601, -3.2150, -1.8292] \text{ km s}^{-1}$  is then taken as the velocity of the whole structure for reconstruction. The inverse direction of  $V_{sc}$ 's projection on the  $L$ - $N_{\max}$  plane is taken as the  $i$  axis. The  $j$  completes the right-hand coordinate system with  $i, k$ . The final reconstruction plane ( $i$ - $j$ ) is found as  $i = [-0.9812, 0.0861, 0.1728]$  and  $j = [0.1878, 0.6336, 0.7506]$ . Note that  $i$  points antisunward,  $j$  is oriented almost along the background magnetic field line, and  $k$  points almost radially outward.

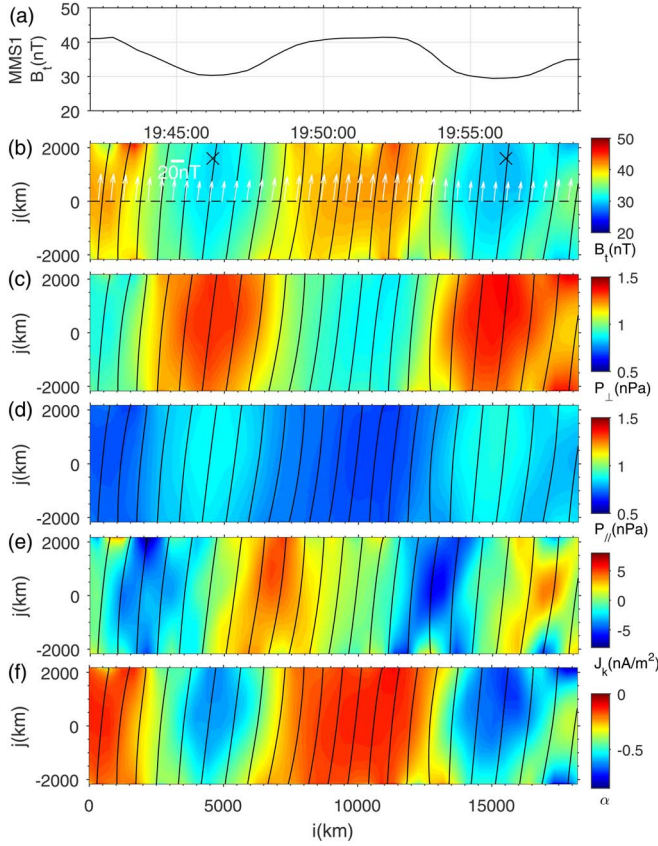
Figure 4 displays the four field-line invariants, namely perpendicular pseudoentropy, parallel pseudoentropy, enthalpy, and  $C_z$  versus the normalized vector potential  $A_0$ , where  $A_0 = -\int B_j di / \max(|-\int B_j di|)$  and  $B_j$  is the  $j$  component of the measured magnetic field. The circles in Figure 4 represent the calculated data, and the gray curves are obtained by polynomial fitting. The four polynomial functions from fitting were used to integrate Equation (2). These curves are single branched, indicating there will be no closed magnetic loop crossed by the path along  $j = 0$  in the  $i$ - $j$  plane. Besides, due to the monotonicity of  $A_0$  in the path, there will also be no reversal of the magnetic lines as in the circumstance of magnetopause crossings (e.g., Hu & Sonnerup 2003).

Figure 5 shows the recovered magnetic field lines and relevant parameters in the  $i$ - $j$  plane. Around  $j = 0$ , a limited domain of  $\pm 2150 \text{ km}$  was recovered because the numerical error will become significant in more distant regions. As shown



**Figure 4.** Four field-line invariants versus the normalized magnetic vector potential  $A_0$ . In each panel, open circles represent the values calculated using the observed data, and the gray line shows the polynomial fitting to the data.

by the black curves, the magnetic field line shows two bottle-like structures, centered around  $i = 4500$  and  $15,000 \text{ km}$ , which are wider near  $j = 0$  and become narrower on both sides. If we take the minimum magnetic field intensity point as the center of the bottle (marked by “ $\times$ ” in Figure 5(b)), the spacecraft passes through the structure  $\sim 1600 \text{ km}$  south of the bottle center. It shows that the azimuthal wavelength of the compressional wave is about  $9000 \text{ km}$ , corresponding to a westward wavenumber of  $m = 44$ . Although the reconstructed region in the  $j$  direction is limited, the lower limit of bottle length (or parallel wavelength) can be estimated to be  $(2150 + 1600) \times 2 = 7500 \text{ km}$  assuming north-south symmetry. Note that the magnetic field intensity at the southernmost part of the magnetic valley region is  $\sim 31 \text{ nT}$  (Figure 5(b)), which is much smaller than the maximum value of  $42 \text{ nT}$  measured during this time interval, indicating that the parallel wavelength of the structure would be much larger than  $7500 \text{ km}$ , which will be discussed in the last section. Opposite to the distribution of magnetic field intensity, the perpendicular and parallel pressures are stronger in the valley region, indicating a state



**Figure 5.** Recovered magnetic field lines and relevant parameters. (a) Total magnetic field strength; the contours in plots (b) to (f) represent the projection of magnetic lines on the  $i$ - $j$  plane with  $B_t$  (b),  $p_{\perp}$  (c),  $p_{\parallel}$  (d),  $J_k$  (e), and  $\alpha$  (f) in color. White arrows in Figure 5(b) represent the magnetic field measured by MMS1 projected in the  $i$ - $j$  plane. The “x” symbols represent the centers of the magnetic bottles and are selected at the point with the lowest magnetic field intensity of each bottle.

of balance (Figures 5(b) and (c)). Figure 5(e) shows the distribution of out-of-plane current density  $J_k$ , whose phase leads  $B_t$  by  $\sim 90^\circ$  and has a maximum value of  $\sim 6 \text{ nA m}^{-2}$  around the magnetic peak–valley boundaries. The causes of this current will be analyzed later. We also note that the anisotropic factor  $\alpha$  is largest in the magnetic valley region and is not field-line invariant as assumed by Teh (2018).

The topology of the magnetic field lines is further analyzed in Figure 6. We choose the data along the path of  $j = -1800, 0, \text{ and } 1800 \text{ km}$  from the reconstructed map (Figure 6(a)) to check the magnitude and phase relationships between  $B_j$  and  $B_i$  (Figures 6(b)–(d)). At  $j = 1800 \text{ and } 0 \text{ km}$ ,  $B_j$  oscillates with an amplitude of  $\sim 6 \text{ nT}$ , while  $B_i$  oscillates with a lower amplitude of  $\sim 2 \text{ nT}$ . At  $j = -1800 \text{ km}$ , the amplitude of  $B_i$  increases to have the same amplitude as the  $B_j$  component of  $\sim 5 \text{ nT}$ . This is consistent with the scenario of a magnetic bottle where the paths of  $j = 1800 \text{ and } 0 \text{ km}$  are closer to the center of the bottle, where the azimuthal component ( $B_i$ ) is weaker while the compressional component ( $B_j$ ) is stronger. The path  $j = -1800 \text{ km}$  is away from the bottle center, where the azimuthal component increases and the compressional component decreases. Furthermore, the phase of  $B_i$  leads  $B_j$  by 90 degrees, indicating sunward (left) propagation of the mirror structures (e.g., Takahashi et al. 1987b). The recovered bottle-like topology is similar to that described in the 2D model proposed by Takahashi et al. (1987a), in which the azimuthal

compression of the magnetic flux provides a source of the compressional component of the wave.

Figure 6(e) shows pressures varying along the magnetic lines in the magnetic trough region at  $\sim i = 4500 \text{ and } 15,000 \text{ km}$ , respectively, as denoted by the dashed and solid lines in Figure 6(a). The more  $j$  increases toward  $\sim 1600 \text{ km}$ , both  $p_{\perp}$  and  $p_{\parallel}$  also show gradual enhancements, being satisfied with the requirements of the magnetic mirror structure. When the mirror structure approaches marginal stability,  $p_{\perp} + \frac{B^2}{2\mu_0}$  should theoretically be constant along the magnetic field line (e.g., Southwood & Kivelson 1993; Kivelson & Southwood 1996). For the first bottle structure (denoted by the dashed line), the value is basically stable, indicating that the structure has reached a saturated stable state. Meanwhile, for the second structure (solid line),  $p_{\perp} + \frac{B^2}{2\mu_0}$  increases gradually for about  $0.05 \text{ nPa}$  from the stronger to the weaker magnetic field region, which may indicate a weak time evolution.

### 4.3. Currents

To illustrate the current system that maintains the magnetic “bottle,” we focus on the time interval between 19:35 and 20:00 UT when the wave has the largest amplitude, as seen in Figure 3(a). The magnetic field disturbances and associated currents in the field-aligned coordinate system are plotted in Figure 7. In this coordinate system, “ $\mathbf{p}$ ” is oriented in the averaged field-aligned direction, “ $\mathbf{a}$ ” points eastward, and “ $\mathbf{r}$ ” completes the right-handed orthogonal system and points radially outward. It shows that the compressional oscillation ( $B_p$ , detrended value) is dominant over the other components (Figure 7(a)). It is known that in an anisotropic and inhomogeneous plasma, the total macroscopic current density ( $J_{\text{all}}$ ) consists of a diamagnetic current ( $J_{\text{dia}}$ ), gradient current ( $J_{\nabla B}$ ), curvature current ( $J_c$ ), and polarization current (Bellan 2008). The first three currents are expressed as follows:

$$J_{\text{dia}} = -\nabla \times \left( \frac{p_{\perp} \hat{B}}{B} \right) \quad (4)$$

$$J_{\nabla B} = -p_{\perp} \frac{\nabla B \times \hat{B}}{B^3} \quad (5)$$

$$J_c = -p_{\parallel} \frac{\hat{B} \cdot \nabla \hat{B} \times \hat{B}}{B^2} \quad (6)$$

where  $\hat{B}$  represents the unit vector of the magnetic field. The polarization current is not considered in the present study because we neglect the change of electric field. These currents are plotted in Figures 7(b)–(d). The contributions of electron pressure to  $p_{\perp}$  and  $p_{\parallel}$  are included in the calculation. It is obvious that both  $J_{\nabla B}$  and  $J_{\text{dia}}$  have extremum at the boundaries between the weak and strong magnetic fields, while the curvature current is relatively weak. Besides, both diamagnetic current and gradient current are dominated by the  $J_r$  component but in opposite directions, and the former is twice as large as the latter in amplitude (up to  $\sim 9 \text{ nA m}^{-2}$ ; Figures 7(b) and (d)). Furthermore, current densities derived from different methods ( $J_{\text{pla}} = N_i e (V_i - V_e)$ ; curlometer method  $\mathbf{J}_B = \nabla \times B / \mu_0$ , Robert et al. 1998; and  $\mathbf{J}_{\text{all}} = \mathbf{J}_{\text{dia}} + \mathbf{J}_{\nabla B} + \mathbf{J}_c$ ) are all displayed in Figures 7(e)–(g) for comparison. The current densities recovered by the reconstruction method (see

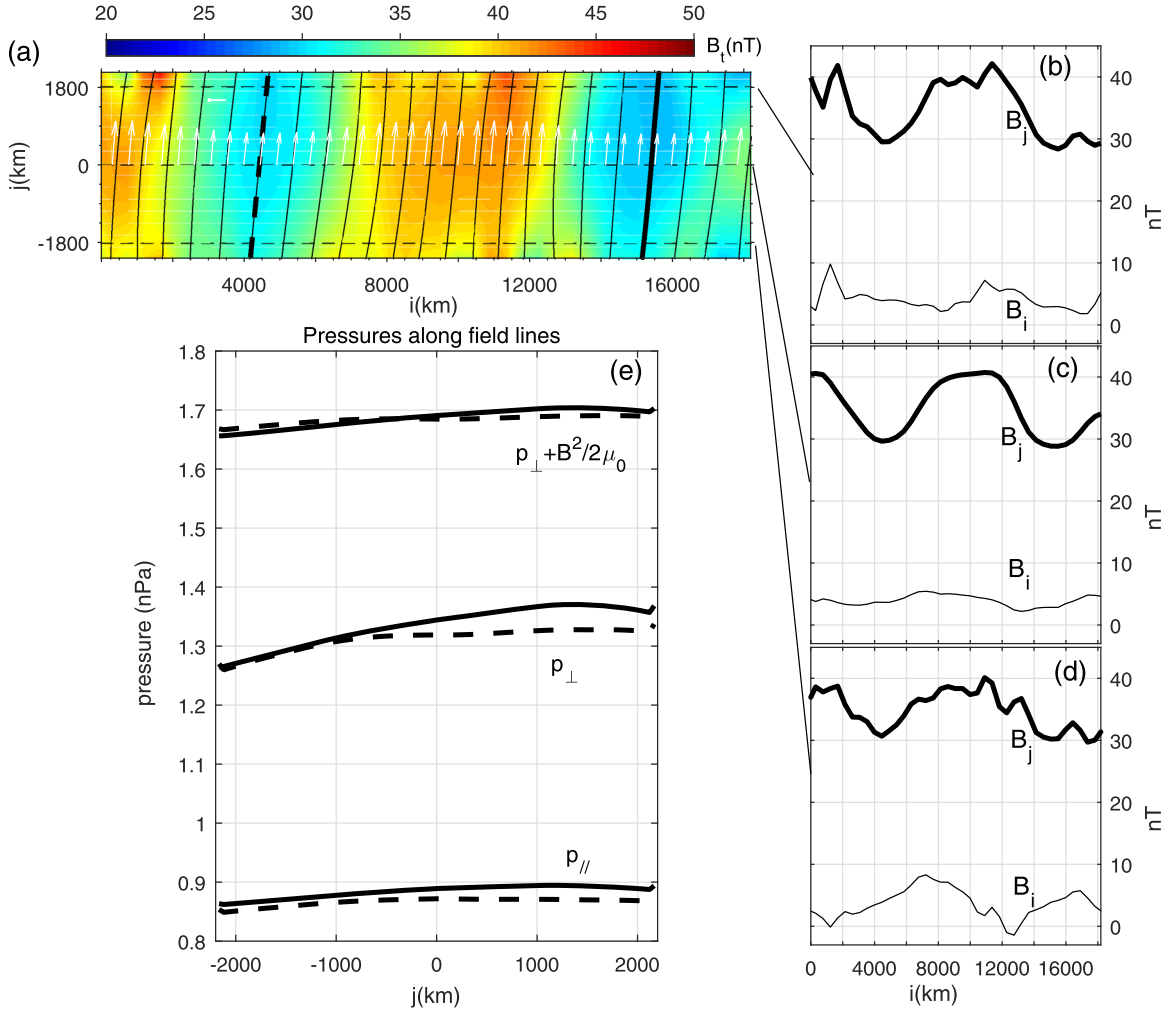


**Figure 6.** (a) Map of the field lines and  $B_t$  in the same format as in Figure 5(b). The three horizontal dashed lines in (a) indicate paths, along which the magnetic field data are extracted and compared in (b)–(d). The thick dashed and solid lines in (a) outline magnetic field lines in the center of each magnetic “bottle,” respectively. The pressures along these two magnetic lines are compared in (e).

Section 4.2) along  $j = 0$  are also projected in field-aligned coordinates and are overplotted in Figures 7(e)–(g) with black curves. We can see that all these currents coincide with each other well, confirming the reliability of each method. In other words, the currents in our event are mainly contributed by diamagnetic and gradient currents, which are oriented almost along or inversely along the radial direction at the boundaries of the magnetic bottles. Considering that the ion temperature is about 7–10 times the electron temperature (Figures 2(d) and (e)), the diamagnetic current is mainly carried by ions. Note that the azimuthal component of  $J_{\text{pla}}$  minus  $2.3 \text{ nA m}^{-2}$  coincides with the current obtained by other methods (Figure 7(f)), indicating that this bias of  $J_{\text{pla}}$  may be due to the systematic errors of the electron velocity  $V_x$  (Figure 3(h)) introduced in the process of photoelectron correction.

#### 4.4. Particle Modulations

The ion differential flux and the pitch angle distributions (PADs) during the time interval from 18:40 to 20:00 UT are shown in Figure 8. The ion flux consists of a hot population from the magnetosphere with energy higher than 1 keV and a cold population with energy less than 100 eV (Figure 8(b)).

The cold components mainly move parallel or antiparallel to the magnetic field line (Figure 8(c)) and are less energetic than those from the sheath (i.e.,  $>100 \text{ eV}$ , Fujimoto et al. 1998), suggesting their origination in the ionosphere. Since the maximum ion flow velocity is  $\sim 40 \text{ km s}^{-1}$  (Figure 3(g)), slower than that of the lowest energy ion we examine (30 eV) at  $\sim 76 \text{ km s}^{-1}$ , the influence of background flow on the PAD could be neglected. From Figures 8(c)–(e), we can see that the PAD of low-energy ions (30–1000 eV) mainly falls in  $0^\circ$ – $30^\circ$  and  $165^\circ$ – $180^\circ$ , the medium-energy ions (2000–6000 eV) are nearly isotropic with weaker PSD near  $90^\circ$ , and the high-energy ions (6000–30,000 eV) show a pancake distribution (PSD peak around  $90^\circ$ ). The above features are typical for magnetospheric plasma PADs (e.g., Zhu & Kivelson 1994). The black curves in Figures 8(c)–(e) show the critical angles of the magnetic mirror calculated using  $\theta_c = \text{asin}(\sqrt{B_t/B_{\text{tmax}}})$ . Particles with pitch angle above the upper one or lower than the bottom one are not trapped (e.g., Yao et al. 2018). The high-energy ions are mainly trapped within the magnetic field trough region, while they are expelled from the strong magnetic field regions (Figure 8(e)). The PAD becomes broader in the magnetic trough regions (Figures 8(a) and (e)), consistent with the scenario of mirror modulation (e.g., Southwood & Kivelson 1993; Kivelson & Southwood 1996; Korotova et al. 2009).

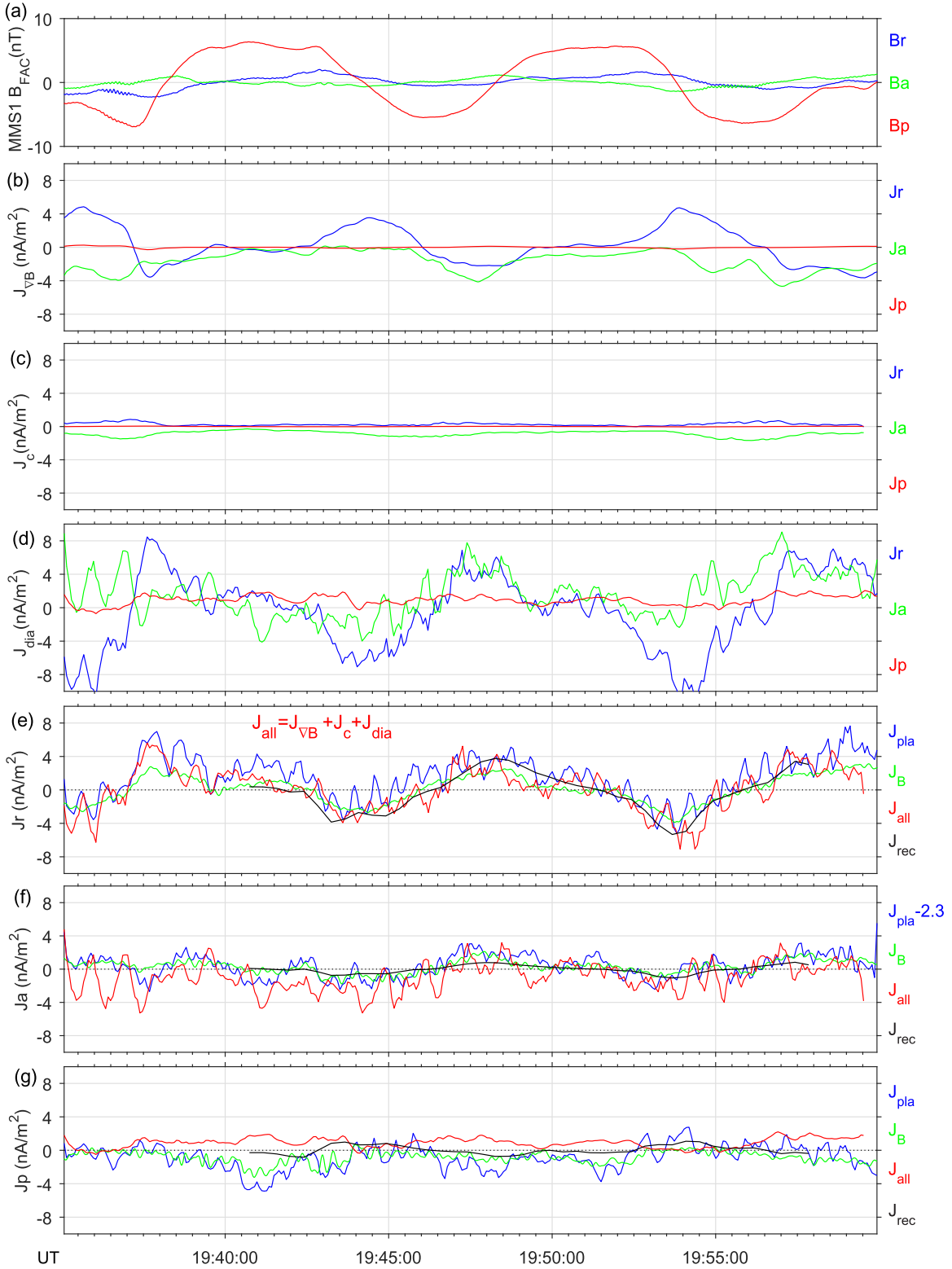


**Figure 7.** Current density obtained by various methods in field-aligned coordinates during 19:35–20:00 UT. (a) Detrended magnetic field data in field-aligned coordinates. Panels (b)–(d) show the gradient current density  $J_{\nabla B}$ , curvature current density  $J_c$ , and diamagnetic current density  $J_{\text{dia}}$  in field-aligned coordinates, respectively. Panels (e)–(g) respectively show the current densities computed from the particle moments ( $J_{\text{pla}}$ ), curlometer ( $J_B$ ), and the sum of ( $J_c$ ,  $J_{\nabla B}$ ,  $J_{\text{dia}}$ ) and the reconstruction method ( $J_{\text{rec}}$ ) in the  $r$ ,  $a$ , and  $p$  directions.

Here  $B_{\text{max}}$  was taken as 42 nT, the maximum value during this time interval, suggesting that the bottle-like structure passed through by the spacecraft may have mirrors with magnetic field magnitude of about 42 nT. In contrast, most of the low- and

middle-energy ions are not or are partially trapped (Figures 8(c) and (d)). Figures 8(f) and (g) show the PSD distributions for ions with center pitch angle at  $\sim 0^\circ$ ,  $90^\circ$ , and  $180^\circ$  around 19:46 UT and 19:52 UT, respectively. We can see that in both the

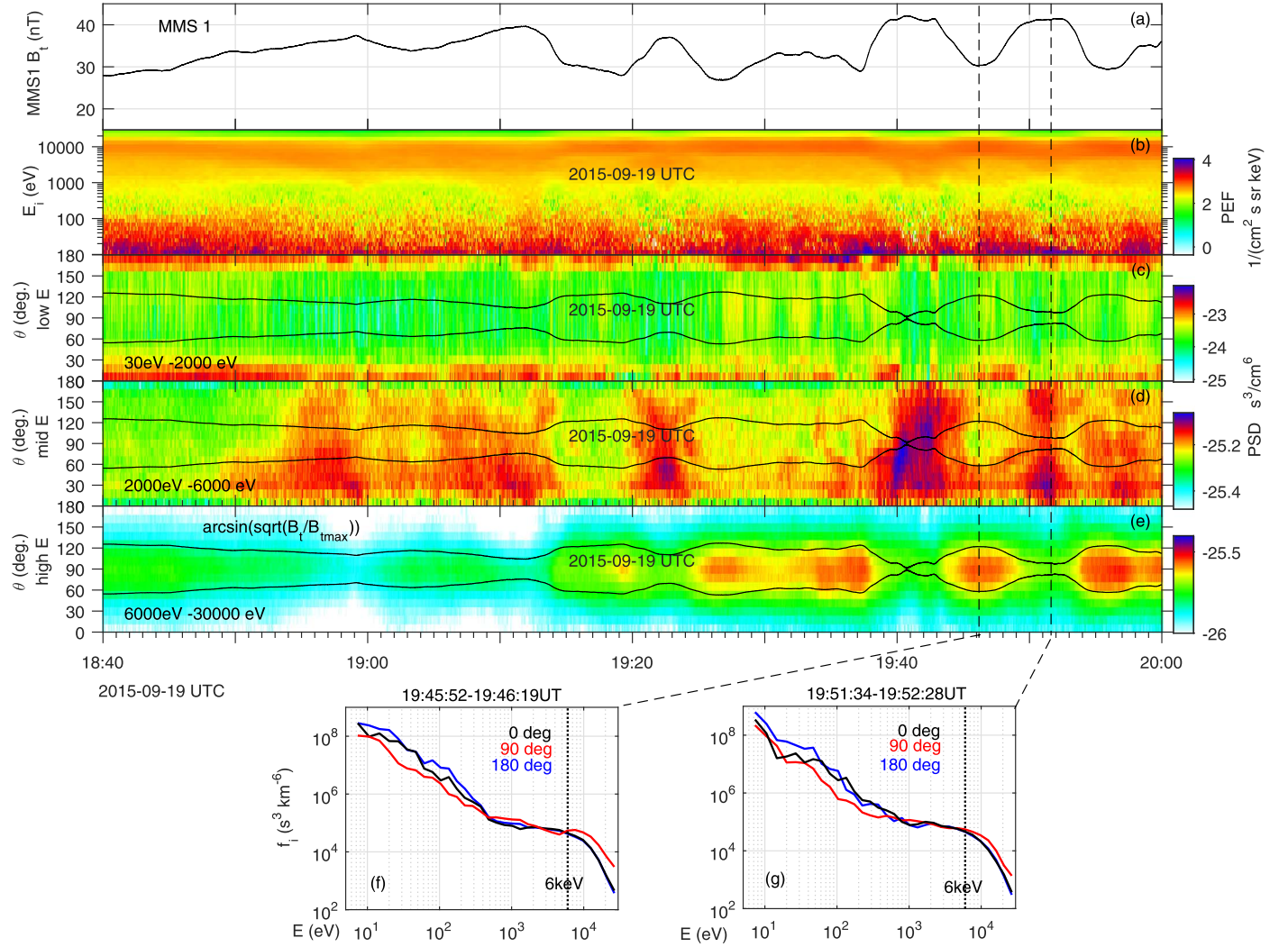


**Figure 8.** Magnetic field and ion data from 18:40 to 20:00 UT observed by MMS1. (a) Total magnetic field strength; (b) ion differential flux. Panels (c)–(e) show the pitch angle distribution for ions with energy of 30–2000 eV, 2000–6000 eV, and 6000–30,000 eV, respectively. The black solid lines are the trapped critical angles for the 6000–30,000 eV ions. Panels (f)–(g) show pitch angle distributions of ions around 0°, 90°, and 180° near the magnetic trough and peak regions, respectively.

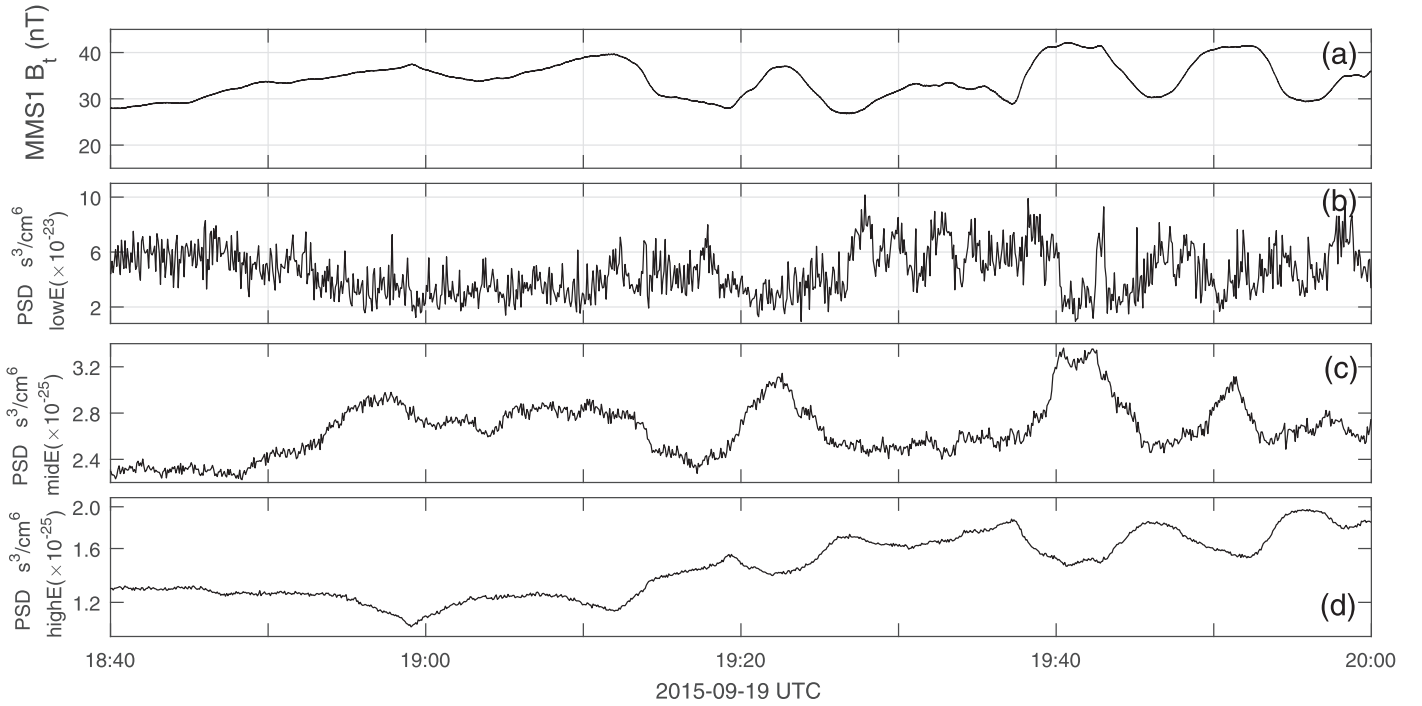
magnetic field trough (19:46 UT) and peak region (19:52 UT), the ion PSD curves with energy larger than 6 keV dominate at  $\sim 90^\circ$ . Therefore, the high-energy population ( $>6$  keV) contributes to the pressure anisotropy required by mirror instability (e.g., Hasegawa 1969; Takahashi et al. 1987b).

Figure 9 shows the variation of omnidirectional PSDs for different energy populations. It shows that the PSD of medium-energy ions oscillates in phase with  $B_t$  (Figure 9(c)), and the PSD of high-energy ions oscillates antiphase with  $B_t$  (Figure 9(d)). The PSD oscillation for low-energy components is somewhat complicated and has a weak positive correlation with the  $B_t$  (Figure 9(b)). Assuming the conservation of both ion magnetic moment ( $\mu$ ) and energy, the PAD-dependent in-phase and antiphase relationships shown in Figure 9 can be explained by the adiabatic motion of particles in the magnetic bottle structure (Zhu & Kivelson 1994; Takahashi et al. 1987b; Liu et al. 2016). Based on the Liouville theorem, Zhu & Kivelson (1994) deduced the formula of the disturbance plasma distribution function as  $\delta f = \mu b_{\parallel} \left( \frac{1}{T_{\perp}} - \frac{1}{T_{\parallel}} \right) f$ , where  $b_{\parallel}$  is the compressional component. Thus, when PAD peaks around  $90^\circ$  ( $T_{\perp} > T_{\parallel}$ ), PSD is antiphase with  $b_{\parallel}$ , and when it peaks far from  $90^\circ$  ( $T_{\perp} < T_{\parallel}$ ), the PAD is in phase with  $b_{\parallel}$ . Note

that the cold ions, with pitch angles close to  $0^\circ$  and  $180^\circ$  (Figure 8(c)), may be less influenced or modulated by the mirror structures.

#### 4.5. Propagation Velocity

The phase velocity of the Pc5 compressional wave provides important information about the generation mechanisms. Figure 10 shows the normal directions ( $N_1$ ) and propagation velocities of seven boundaries in the Pc5 wave by using the STD method. The arrows in Figures 10(b) and (c) represent the normal directions of these boundaries in the GSE  $X$ - $Y$  and  $X$ - $Z$  planes. It can be seen that except for the second boundary, the propagation directions are sunward (westward;  $V_{N_1} > 0$ ). Note also that the normal component of the background plasma velocity (green curves) is almost identical to the normal velocity obtained by STD (blue curves, Figure 10(d)) with values of  $10$ – $40 \text{ km s}^{-1}$ , which indicates that the observations of an oscillatory magnetic field and other parameters are caused by a quasi-stationary structure passing through the spacecraft sunward along with the drifting plasma. These results are a manifestation of the drift-mirror mode but exclude the possibility of the slow mode. In addition, what is unexpected



**Figure 9.** Total magnetic field strength  $B_t$  (a) and the variation of omnidirectional phase space density for low-energy (30–2000 eV) (b), medium-energy (2000–6000 eV) (c), and high-energy (6000–30,000 eV) (d) ions observed by MMS1.

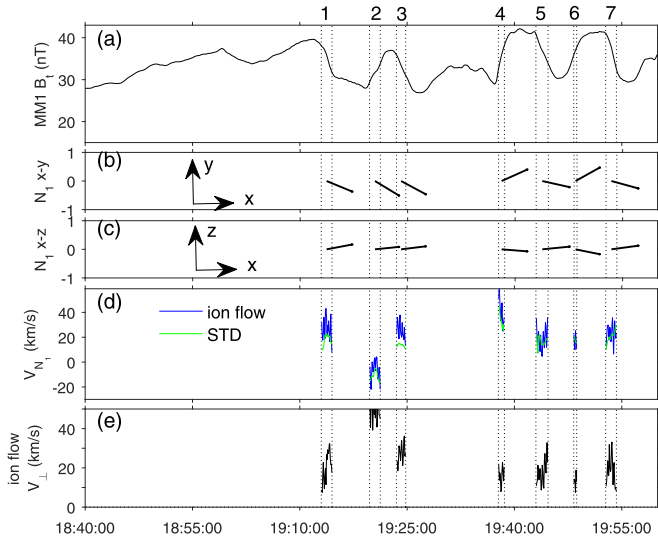


**Figure 10.** Velocities of/at the wave boundaries in the spacecraft frame. (a) Total magnetic field strength observed by MMS1. (b)–(c) Unit normal vectors of the wave boundaries in the  $x$ – $y$  (b) and  $x$ – $z$  (c) planes. (d) Normal velocities calculated by STD (green) and from the ion velocities (blue). (e) Perpendicular components of the ion velocities to the normal directions of these boundaries. The vertical dashed lines mark the time intervals for calculating velocities at the corresponding boundaries.

is that the normal vectors of the leading and trailing boundaries of the magnetic field enhancement, such as the boundaries of 4–5 or 6–7 in Figure 10(b), swing in the radial direction ( $y$ ), indicating that the radial scale of the magnetic “bottle” would be limited, which has been neglected in the reconstruction process of this paper. The detailed radial configuration of the mirror-like structure will be studied using multispacecraft observations in our further work.

## 5. Discussion

The choice of proper frame and whether the structure is magnetohydrostatic will affect the accuracy of the reconstruction results (e.g., Hau & Sonnerup 1999; Sonnerup et al. 2006). The deHoffmann–Teller (HT) frame (Khrabrov & Sonnerup 1998) is usually chosen as the proper frame. Sometimes it is not ideal or appropriate for a slowly evolving structure; thereby the initial data taken by the spacecraft would be aliased by both spatial and temporal effects. Ideally, magnetic and plasma variations purely due to spatial variation are needed as spatial initial values for reconstruction at a given time. Hasegawa et al. (2014) have developed a useful method for decomposing spatial and temporal variations from single-spacecraft data under a set of assumptions, including (1) a frozen-in condition exists, (2) the density and temperature are field-line invariants, and (3) the pressure is isotropic (Sonnerup & Hasegawa 2010; Hasegawa et al. 2010, 2014). Unfortunately, these assumptions are not satisfied by our event. Nevertheless, we note that previous studies have shown that the structure of Pc5 compressional waves of the type observed in this study are generally stable on minute timescales. From multipoint observations by Time History of Events and Macroscale Interaction during Substorms (THEMIS), Constantinescu et al. (2009) found that there are few changes in the wave form for a timescale of minutes and distances of the order of 10,000 km. For our event, considering the almost-constant total pressure  $p_{\text{tot}}$  ( $\sim 1.5$  nPa, Figure 3(f)) and the three boundaries with nearly common normal directions and speeds of  $\sim 20$  km  $s^{-1}$  (Figures 10(b)–(d)) in the spacecraft frame, it can be inferred that the structure does not experience monotonous expansion or contraction during the reconstructed time interval from 19:40:15 to 19:59:10 UT. Besides, given the simple topology of the magnetic bottle, we consider that ignoring slow temporal effects would not change the shape of the bottle significantly. A

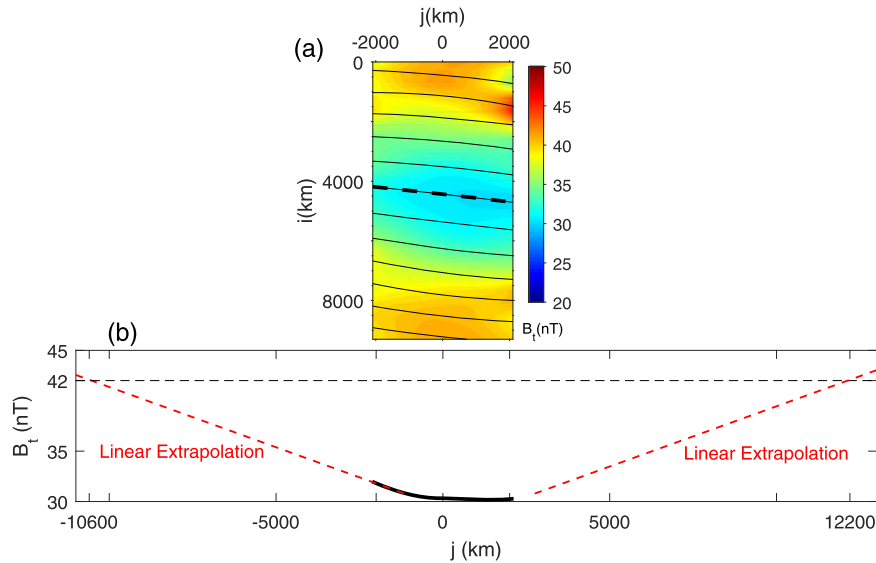


**Figure 11.** Estimation of the scale of the mirror structure along the magnetic field line. Panel (a) displays the first magnetic bottle shown in Figure 5(b). The black curve in (b) shows the variation of magnetic field intensity along the center magnetic field line as marked by the dashed line in (a). The red dashed line in (b) shows data from linear extrapolation. The end points of the magnetic mirror are selected at positions with magnetic field intensity of 42 nT.

useful way to track the time evolution of the magnetic structure is to compare measurements from multiple spacecraft. However, the spacecraft separation of our event is too small ( $\sim 60$  km) to find obvious differences between them. Since the separation is comparable to the integration step ( $\sim 46$  km) in the  $j$  direction, magnetic field data predicted by reconstruction with MMS1 data matched very well ( $>99\%$  correlation) with that observed by MMS2–4 (not shown). How Pc5 compressional waves propagate and evolve remains to be studied by spacecraft with an appropriate separation distance and will hopefully be addressed in future studies.

We have calculated the drift velocity that is due to curvature, gradient, and diamagnetic effects, and we find it has a strong radial component of  $\sim 20$  km s $^{-1}$  at the magnetic bottle boundaries. This contributes to most of the measured tangential ion velocities as shown in Figure 10(e), suggesting that the plasma is not frozen-in, due to the strong magnetic field and thermal pressure gradient near the boundaries. Therefore, the measured ion velocity should not be used in the HT analysis (Khrabrov & Sonnerup 1998). On the other hand, the STD method would give a more reliable structure velocity. In addition, in the frame of the magnetohydrostatic structure, the inertia term in the momentum equation can be ignored (e.g., Hau & Sonnerup 1999). In our event, the flow speed is less than 40 km s $^{-1}$  (Figure 3(g)), much lower than that of the local Alfvén speed of  $\sim 712$  km s $^{-1}$  (by using  $B = 35$  nT,  $N_i = 1.15$  cm $^{-3}$ ), suggesting that it is reasonable to ignore the inertia term in our reconstruction.

The field-aligned scale and possible generation mechanisms of the present Pc5 compressional wave event are discussed below. The azimuthal size of  $\sim 9000$  km for our event is comparable to the typical scale of several Re as reported in previous works (e.g., Zhu & Kivelson 1994; Vaivads et al. 2001). Both empirical 2D or 3D sketches (e.g., Takahashi et al. 1987a; Haerendel et al. 1999) and the theory of an antisymmetric drift-mirror ballooning mode (Cheng & Qian 1994; Sibeck et al. 2012) suggest that the Pc5 compressional waves behave like a standing wave structure, with the compressional component, the thermal pressure, antisymmetric with respect to the equatorial plane. However, due to limited spatial coverage, only a few observations have been done on the

field-aligned structure accompanied by the Pc5 waves (e.g., Takahashi et al. 1987a; Korotova et al. 2013). Using THEMIS observations, the meridional wavelength of a compressional poloidal wave was estimated to exceed 3Re (Korotova et al. 2013).

Our reconstruction maps depicted the wave structure along the magnetic field line in a domain of  $\sim 4000$  km, showing two “bottle-like” structures independent of any model constraint (Figures 5 and 11). However, due to numerical errors and 3D effects along magnetic field lines, the whole profile of the bottles cannot be covered (e.g., Sonnerup et al. 2006; Tian et al. 2019). We extract the first magnetic bottle (Figure 11(a)) and try to extrapolate it to get its length in the field-aligned direction (nearly along the  $j$  axis). The black curve in Figure 11(b) shows the variation of the magnetic field intensity along the center magnetic field line, as marked by the black dashed line in Figure 10(a). It can be seen that  $B_t(j)$  varied almost linearly with  $j$  between  $j = -1000$  km and  $-2000$  km. We extrapolate this linear trend and take the mirror intensity as 42 nT and let  $B_t(j_{\min}) = 42$  nT, and then we get  $J_{\min} = -10,600$  km. If we further assume that the magnetic bottle is symmetrical with respect to its center in the field-aligned direction, the bottle length is estimated to be  $\sim 3.6$  Re, much larger than the azimuthal scale, consistent with previous observations (e.g., Zhu & Kivelson 1994).

Note that we made a rough estimation for the field-aligned size under the assumptions, where the magnetic bottle is not necessarily centrosymmetric, and the magnetic field intensity at the magnetic mirror point may also be underestimated. Considering the position of the spacecraft, the center of the magnetic bottle is located about 3.4 Re southward from the magnetic equatorial plane, indicating an antisymmetric structure with respect to the equatorial plane. Furthermore, no frequency doubling is seen in the compressional component of the magnetic field, which also means that the observation is made far away from the equatorial plane (see Figure 7(a)). Because phenomena of frequency doubling in the compressional oscillation are frequently observed near the equatorial plane (e.g., Sibeck et al. 2012; Korotova et al. 2013), which has been attributed to the north/south oscillations in the latitude of

the equatorial node of the field-line displacement (Takahashi et al. 1987a).

The antisymmetric ballooning-mirror mode theoretically exhibits a strong coupling between the transverse and parallel magnetic components when the mirror instability condition is satisfied near the equator (Cheng & Qian 1994). In this mode, the Br and Bp components are predicted to oscillate in phase in the south hemisphere. However, this phase relationship is not obvious in our observations (see Figure 7(a)). Nevertheless, the possibility of a ballooning-mirror mode cannot be ruled out as a generation mechanism for our event, because in this mode the Br amplitude will decrease greatly away from the equatorial plane, as the simulation suggested. Another possibility is that the mirror mode is dominant over the ballooning mode in our event.

The OMNI data showed that the interplanetary magnetic field Bz (GSM) changed from 2 nT to weakly southward, the SYM-H index increased from  $-12$  to  $-2$  nT, and the AE index increased from 40 nT to 80 nT during 19:10 UT to 20:00 UT, when MMS observed obvious compressional waves (Figure 3), indicating the occurrence of a weak substorm. It could be inferred that the sudden increase (about  $1.4\times$ ) in perpendicular ion temperature after 19:10 UT (Figure 3(d)) may be caused by the substorm injections from the tail (e.g., Takahashi et al. 1987b). Then the enhanced ion beta and anisotropy would enable the excitation of the drift-mirror or ballooning-mirror instabilities in the duskside outer magnetosphere. In other words, drift-mirror-like instabilities could be possible generation mechanisms for the Pc5 compressional wave.

## 6. Summary

Based on data from the MMS spacecraft, we analyzed in detail a Pc5 compressional event in the duskside southern hemisphere on 2015 September 19. This event, nearly pressure balanced, occurred in a plasma environment with high  $\beta$  ( $\beta_{\perp} \sim 2.5$ ) and obvious temperature anisotropy ( $T_{i\perp}/T_{i\parallel} \sim 1.5$ ). A GS-like method including pressure anisotropy based on the reduced equations from Sonnerup et al. (2006) is first applied to recover the topology of the wave structure. The reconstruction map shows that the compressional wave has bottle-like structures. The spacecraft passes through the structures at the south side of the bottles. A rough estimation of the length of the magnetic bottle is close to 3.6 Re, much larger than the azimuthal size of  $\sim 9000$  km. Other multispacecraft analysis methods are adopted to quantify the currents and phase velocities of this wave. The generation of this Pc5 compressional wave could be related to drift-mirror-like instabilities.

This work was supported by the Shandong University (Weihai) Future Plan for Young Scholars (2017WHWLJH08). This work was also supported by the Swedish National Space Agency (SNSA) grant 118/17 and the Natural Science Foundation China (NSFC) grant 41750110486. A.M.T. thanks Qiang Hu for useful discussions on the benchmark of the relevant methods. We thank the MMS mission team for providing high-quality data. The MMS data used can be downloaded at <https://lasp.colorado.edu/mms/sdc/public/>.

## ORCID iDs

Anmin Tian  <https://orcid.org/0000-0002-4351-551X>

## References

- Bellan, P. M. 2008, *Fundamentals of Plasma Physics* (Cambridge: Cambridge Univ. Press)
- Burch, J. L., Moore, T. E., Torbert, R. B., et al. 2016, *SSR*, **199**, 5
- Chen, G.-W., & Hau, L.-N. 2018, *JGRA*, **123**, 7358
- Cheng, C. Z., & Qian, Q. 1994, *JGR*, **99**, 11193
- Constantinescu, O. D., Glassmeier, K.-H., Plaschke, F., et al. 2009, *JGRA*, **114**, A00C25
- Denton, R. E., Sonnerup, B. U. Ö, Hasegawa, H., et al. 2016, *GRL*, **43**, 5589
- Fujimoto, M., Terasawa, T., Mukai, T., et al. 1998, *JGR*, **103**, 4391
- Gershman, D. J., Avannov, L. A., Boardsen, S. A., et al. 2017, *JGRA*, **122**, 11548
- Haerendel, G., Baumjohann, W., Georgescu, E., et al. 1999, *AnGeo*, **17**, 1592
- Hasegawa, A. 1969, *PhFI*, **12**, 2642H
- Hasegawa, H., Sonnerup, B. U. Ö, Denton, R. E., et al. 2017, *GRL*, **44**, 4566
- Hasegawa, H., Sonnerup, B. U. Ö, & Hu, Q. 2014, *JGRA*, **119**, 97
- Hasegawa, H., Sonnerup, B. U. Ö, Klecker, B., et al. 2005, *AnGeo*, **23**, 973
- Hasegawa, H., Nakamura, R., Fujimoto, M., et al. 2007, *JGRA*, **112**, A11206
- Hasegawa, H., Sonnerup, B. U. Ö, & Nakamura, T. 2010, *JGRA*, **115**, A11219
- Hau, L.-N. 1996, *PhPI*, **3**, 1113
- Hau, L. N., & Sonnerup, B. U. Ö 1999, *JGR*, **104**, 6899
- Hau, L. N., Phan, T. D., Sonnerup, B. U. Ö, & Paschma, G. 1993, *GRL*, **20**, 2255
- Hu, Q., & Sonnerup, B. U. Ö 2002, *JGRA*, **107**, 1142
- Hu, Q., & Sonnerup, B. U. Ö 2003, *JGRA*, **108**, 1011
- Jing, H., Lu, J. Y., Kabin, K., et al. 2014, *P&SS*, **97**, 50
- Khrabrov, A. V., & Sonnerup, B. U. Ö 1998, in *Analysis Methods for Multi-Spacecraft Data*, ed. G. Paschmann & P. W. Daly (New York: Springer), 221
- Kivelson, M. G., & Southwood, D. J. 1996, *JGR*, **101**, 17365
- Korotova, G. I., Sibeck, D. G., Angelopoulos, V., & Walsh, B. M. 2013, *JGRA*, **118**, 7665
- Korotova, G. I., Sibeck, D. G., Kondratovich, V., et al. 2009, *AnGeo*, **27**, 3725
- Liu, H., Zong, Q. G., Zhou, X. Z., et al. 2016, *JGRA*, **121**, 6262
- Lu, J. Y., Rankin, R., Marchand, R., et al. 2003, *GRL*, **30**, 1540
- Pollock, C., Moore, T., Jacques, A., et al. 2016, *SSRv*, **199**, 331
- Robert, P., Dunlop, M. W., Roux, A., & Chanteur, G. 1998, in *Analysis Methods for Multi-Spacecraft Data*, ed. G. Paschmann & P. W. Daly (New York: Springer), 395
- Russell, C. T., Anderson, B. J., Baumjohann, W., et al. 2016, *SSRv*, **199**, 189
- Shi, Q. Q., Hartinger, M., Angelopoulos, V., et al. 2013, *JGRA*, **118**, 284
- Shi, Q. Q., Shen, C., Dunlop, M. W., et al. 2006, *GRL*, **33**, L08109
- Shi, Q. Q., Shen, C., Pu, Z. Y., et al. 2005, *GRL*, **32**, L12105
- Shi, Q. Q., Tian, A. M., Bai, S. C., et al. 2019, *SSR*, **215**, 35
- Shi, Q. Q., Zong, Q.-G., Zhang, H., et al. 2009, *JGRA*, **114**, A12219
- Shue, J. H., Song, P., Russell, C. T., et al. 1998, *JGR*, **103**, 17691
- Sibeck, D. G., Korotova, G., Turner, D. L., et al. 2012, *JGR*, **117**, A11215
- Sonnerup, B. U. Ö, & Guo, M. 1996, *GRL*, **23**, 3679
- Sonnerup, B. U. Ö, & Hasegawa, H. 2010, *JGR*, **115**, A11218
- Sonnerup, B. U. Ö, Hasegawa, H., Teh, W. L., & Hau, L. N. 2006, *JGR*, **111**, A09204
- Sonnerup, B. U. Ö, & Hau, L. N. 1994, *JGR*, **99**, 143
- Southwood, D. J., Dungey, J. W., & Etherington, R. J. 1969, *P&SS*, **17**, 349
- Southwood, D. J., & Kivelson, M. G. 1993, *JGR*, **98**, 9181
- Su, S. Y., Konradi, A., & Fritz, T. A. 1977, *JGR*, **82**, 1859
- Su, S.-Y., McPherron, R. L., Konradi, A., et al. 1980, *JGR*, **85**, 515
- Takahashi, K., Fennell, J. F., Amata, E., & Higbie, P. R. 1987a, *JGR*, **92**, 5857
- Takahashi, K., Higbie, P. R., & Baker, D. N. 1985, *JGR*, **90**, 1473
- Takahashi, K., Lopez, R. E., McEntire, R. W., et al. 1987b, *JGR*, **92**, 13472
- Teh, W.-L. 2018, *EP&S*, **70**, 34
- Teh, W.-L. 2019, *JGRA*, **124**, 1644
- Tian, A. M., Shi, Q. Q., Degeling, A. W., & Zhang, S. 2019, *Science China Technological Sciences*, **62**, 1003
- Tian, A. M., Zong, Q.-G., & Shi, Q. Q. 2012, *Science China Technological Sciences*, **55**, 1092
- Vaivads, A., Baumjohann, W., Haerendel, G., et al. 2001, *AnGeo*, **19**, 311
- Xiao, T., Shi, Q. Q., Zhang, T. L., et al. 2010, *AnGeo*, **28**, 1695
- Yang, B., Zong, Q.-G., Wang, Y. F., et al. 2010, *JGRA*, **115**, A02214
- Yao, S. T., Shi, Q. Q., Liu, J., et al. 2018, *JGRA*, **123**, 5561
- Yao, S. T., Wang, X. G., Shi, Q. Q., et al. 2017, *JGRA*, **122**, 1990
- Zhu, X. M., & Kivelson, M. G. 1991, *JGR*, **96**, 19451
- Zhu, X. M., & Kivelson, M. G. 1994, *JGR*, **99**, 241
- Zong, Q.-G., Zhou, X.-Z., Li, X., et al. 2007, *GRL*, **34**, L12105
- Zong, Q.-G., Zhou, X.-Z., Wang, Y. F., et al. 2009, *JGRA*, **114**, A10204